

1 **Effects of Mass Ratio Heterogeneity and Coating-Related Optical**
2 **Characteristics on the Light Absorption Enhancement of Black Carbon-**
3 **Containing Particles**

4 **Jing Wei¹, Jin-Mei Ding², Yao Song¹, Xiao-Yuan Wang², Xiang-Yu Pei¹, Sheng-**
5 **Chen Xu², Fei Zhang¹, Zheng-Ning Xu¹, Xu-Dong Tian², Bing-Ye Xu², Zhi-Bin**
6 **Wang^{1,3}**

7 ¹ State Key Laboratory of Soil Pollution Control and Safety, Zhejiang Provincial Key
8 Laboratory of Organic Pollution Process and Control, College of Environmental and
9 Resource Sciences, Zhejiang University, Hangzhou 310058, China

10 ² Ecological and Environmental Monitoring Center of Zhejiang Province, Hangzhou
11 310012, China

12 ³ ZJU-Hangzhou Global Scientific and Technological Innovation Center, Zhejiang
13 University, Hangzhou 311200, China

14 **Correspondence:** Bing-Ye Xu (xubingye@zjemc.org.cn) and Zhi-Bin Wang
15 (wangzhibin@zju.edu.cn)

16

17 **Abstract**

18 Black carbon (BC) is a strong climate forcer, but considerable uncertainty remains in
19 estimating its radiative impact, largely due to persistent gaps between observed and
20 modeled light absorption enhancement (E_{abs}). In this study, we employed a Centrifugal
21 Particle Mass Analyzer and Single Particle Soot Photometer tandem system to
22 characterize mass ratio (M_{R} , coating-to-BC) of BC-containing particles in Hangzhou,
23 China. Observations across a field campaign revealed low, medium, and high E_{abs}
24 values under varying atmospheric conditions. The uniform core-shell Mie model
25 overestimated E_{abs} , particularly during clean periods (low E_{abs}). To address this, we
26 developed an observationally constrained parameterization for transition-state particles
27 based on M_{R} -dependent optical transitions behaviors. This approach effectively
28 reconciles modeled and measured E_{abs} across varying pollution conditions. It also
29 emphasizes the importance of incorporating M_{R} heterogeneity and transition-state
30 optical behavior to improve BC light absorption estimates and reduce uncertainties in
31 assessing radiative effects.

32 **1 Introduce**

33 Black carbon (BC) is a strongly light-absorbing aerosol that effectively absorbs
34 solar radiation, warms the atmosphere, and contributes to direct radiative forcing (DRF)
35 (Bond and Bergstrom, 2006; Seinfeld, 2008). According to IPCC assessments, the
36 global effective DRF of BC ranges from -0.28 to 0.41 W/m^2 (Szopa et al., 2021). To
37 represent the effect of BC particle coatings on absorption, most climate models (Bauer
38 et al., 2013; Chen et al., 2024; Stier et al., 2005; Wang et al., 2023; Zhang et al., 2025b)
39 estimate BC light absorption enhancement (E_{abs}) using Mie theory, defined as the ratio
40 of absorption by coated BC to that of uncoated BC cores, under the assumption of a
41 uniform core-shell structure where BC core is fully encapsulated by coating materials.
42 This approach predicts a monotonic increase in E_{abs} with the coating-to-core mass ratio
43 (M_{R}), often reaching values up to ~ 2 , consistent with laboratory results (Peng et al.,
44 2016) and the pyroCb smoke (Beeler et al., 2024). However, field observations
45 commonly report lower E_{abs} values, typically around 1.4 and sometimes as low as 1.09
46 (Cappa et al., 2012; Huang et al., 2024), although some studies have found moderate
47 E_{abs} values, with maxima reaching approximately 1.5 (Liu et al., 2015b). This
48 discrepancy mainly stems from the oversimplified assumptions in Mie theory, which
49 fail to capture the real atmospheric complexity in BC size distribution, coating
50 configuration, and mixing state (Wang et al., 2021c). Previous microscopy-based
51 single-particle studied (e.g., TEM and SEM) have visually demonstrated that the
52 ambient BC particles exhibit diverse coating structures and highly heterogeneous
53 mixing states, providing direct evidence of deviation from the idealized core-shell
54 assumption (Adachi et al., 2010; Adachi and Buseck, 2013; China et al., 2013; Wang et
55 al., 2021c). Although microscopy techniques are not employed in this work, these
56 findings highlight the importance of realistically representing BC mixing state and
57 coating characteristics when modeling optical properties. The mismatch between model
58 assumptions and observations has motivated efforts to refine the conceptual modeling
59 approaches for BC aging and coating evolution, which forms the focus of this study.

60 A number of studies have explored the discrepancies in BC E_{abs} from various
61 perspectives. Particle-resolved modeling has demonstrated that both particle-to-particle
62 heterogeneity in M_R and deviations from the idealized core-shell structure can strongly
63 influence absorption estimates (Fierce et al., 2020). In particular, non-uniform or partial
64 coatings at low M_R can lead to the overestimation of E_{abs} by traditional core-shell
65 models. However, these factors alone tend to cannot explain the low E_{abs} frequently
66 observed under high M_R conditions (Huang et al., 2024). Atmospheric BC particles also
67 exhibit substantial variability in their internal mixing state during aging. Fresh BC
68 exhibit a branched structure that collapses into compact shapes with reduced light
69 absorption cross-sections during aging (Moteki and Kondo, 2007; Romshoo et al., 2024;
70 Li et al., 2024; Radney et al., 2014; Corbin et al., 2023). Early aging stage feature
71 uneven coatings, while aged particles show BC core either encapsulated or located near
72 the particle surface (Zhang et al., 2008; Adachi and Buseck, 2013). These aging features
73 are consistent with single-particle observations showing the progressive collapse and
74 coating thickening of BC aggregates during atmospheric processing (Adachi et al., 2016;
75 Ueda et al., 2016), which support the conceptual framework adopted in this study.
76 Recent studies further suggest that the proportion of non-spherical BC particles and the
77 position of the BC core may be key factors contributing to low E_{abs} , leading to an
78 overestimation by core-shell model (Huang et al., 2024; Chen et al., 2024; Zhang et al.,
79 2022). Although this study does not involve direct microscopic measurements or
80 detailed particle-resolved modeling, our work aims to refine the conceptual
81 representation of BC aging and coating evolution to better capture M_R -related optical
82 behavior under ambient conditions.

83 In this study, a suite of state-of-the-art instruments were employed to
84 simultaneously capture the magnitude and temporal of BC M_R in Hangzhou, China
85 (Zhang et al., 2025a; Qian et al., 2025). The ratio of SP2-measured single-particle
86 scattering cross sections to the core-shell Mie theory simulated values was used as an
87 observational proxy to characterize M_R -dependent optical transitions of BC-containing
88 particles (Liu et al., 2017a; Liu et al., 2020). Field measurements revealed the
89 coexistence of high, medium, and low E_{abs} under high bulk-averaged M_R conditions.
90 Based on these observations, the influences of M_R heterogeneity and M_R -dependent
91 optical behavior were quantified to reconcile discrepancies in E_{abs} between model
92 predictions and field observations. Subsequently, an observationally constrained
93 parameterization for “transition-state” BC-containing particles was refined to better
94 reproduce measured E_{abs} under different ambient atmospheric conditions. This study
95 underscores the importance of simultaneously accounting for M_R heterogeneity and M_R -
96 dependent optical transitions when predicting E_{abs} , offering insights that can help reduce
97 uncertainties in estimates of BC direct radiative forcing.

98 **2 Methods**

99 **2.1 Overview of the field campaign and instrumentation**

100 The field measurements were conducted at the Central Air Quality Assurance
101 Monitoring Station (30.25°N, 120.24°E) in Hangzhou from 3th Sept., 2023 to 13th Oct.,

102 2023. The sampling site is located just 100 meters from the Qiantang River in the
103 western part of Hangzhou, with major traffic routes within 3 kilometers to the northeast
104 and southwest of the station. The schematic of the instrumentation is provided in Fig.
105 S1. Aerosols were sampled after passing through a PM_{2.5} impactor and then dried
106 through a diffusion dryer before reaching subsequent instruments.

107 The mass of a BC-containing particle (M_p) and of the BC core (M_{BC_core}) were
108 simultaneously obtained by a Centrifugal Particle Mass Analyzer (CPMA, Cambustion)
109 and a single-particle soot photometer (SP2, DMT Inc.) tandem system. The CPMA
110 classifies particles according to their total mass and has been described in detail by
111 Olfert and Collings (2005). According to the instrument manual, the mass accuracy of
112 the CPMA is approximately 5%. The SP2 measures particle incandescence and
113 scattering to determine BC core mass and optical properties (Stephens et al., 2003;
114 Moteki and Kondo, 2010; Gysel et al., 2011; Schwarz et al., 2022), and the uncertainty
115 associated with the SP2-derived BC core mass (M_{BC_core}) is approximately 10%
116 (Laborde et al., 2012). Previous studies have applied the tandem CPMA-SP2 set up
117 (Cross et al., 2010; Liu et al., 2022; Naseri et al., 2022; Zanatta et al., 2025). In this
118 work, SP2 was calibrated using size-resolved Aquadag aerosols (DMT, 2011) (Fig. S2c
119 and d) following the procedures described by Baumgardner et al. (2012) and Laborde
120 et al. (2012). In this setup, particles with known mass (M_p) selected by CPMA were
121 injected into the SP2.

122 The CPMA was operated over M_p setpoints ranging from 0.9 fg to 30 fg,
123 logarithmically spaced into ten intervals (0.93 fg, 1.37 fg, 2.02 fg, 2.97 fg, 4.36 fg, 6.40
124 fg, 9.39 fg, 13.78 fg, 20.22 fg and 29.68 fg), then the mass of BC core was measured
125 by SP2. The duration of one set point cycle was 1 hour, with each M_p point sampling
126 for 5 minutes, and all M_p points was sampling for total of 50 minutes. The remaining
127 10 minutes were divided into 4 minutes for instrument stabilization and 6 minutes for
128 measuring all BC-containing particles when the valve was switched to the single SP2
129 line. During further data analysis, particles with $M_p = 0.93$ fg and $M_p = 1.37$ fg exhibited
130 excessively noisy scattering signals, likely due to weak signal intensity and low signal-
131 to-noise ratio for small particles, and were therefore excluded from subsequent
132 statistical analysis.

133 In the subsequent data processing, measurements from the CPMA-SP2 system
134 were first corrected for multiple charging effects using a peak-resolved subtraction
135 approach. An X-ray aerosol neutralizer (TSI 3088) installed upstream of the CPMA
136 produced a known bipolar charge distribution, resulting in discrete mass modes
137 corresponding to singly and multiply charged particles in the CPMA mass spectra. The
138 CPMA transfer function was calculated based on the CPMA geometric and operational
139 parameters, with a set mass resolution $R_m=8$ (Text S1), ensuring that charge-dependent
140 mass modes were sufficiently resolved. Under these conditions, mass peaks attributable
141 to multiply charged particles ($q > 1$) could be explicitly identified based on their
142 expected mass-to-charge relationships and quantitatively subtracted, while the singly
143 charged mode corresponding to the CPMA setpoint was retained for subsequent
144 analysis. This peak-resolved subtraction represents a simplified, charge-resolved
145 inversion, which differs from full matrix-based inversion schemes (Naseri et al., 2024;

146 Naseri et al., 2021) , but is appropriate when charge-dependent mass modes are well
147 resolved and non-overlapping. Additional corrections, including SP2 detection
148 efficiency, and instrumental time delay, were applied as described in Text S1. The mass
149 of each BC core (M_{BC_core}) was then calculated from the SP2 incandescence signal using
150 the calibration described above, with a correction factor of 0.75 applied to the peak
151 height (Liu et al., 2020; Liu et al., 2014; Zhang et al., 2018; Gysel et al., 2011). The
152 SP2 scattering signal was calibrated with polystyrene latex spheres (PSL) of known
153 sizes (210 nm, 270 nm and 310 nm) (Fig. S2b). Additionally, the calibration of the
154 scattering and the incandescence channels was performed before and after the
155 measurement campaign.

156 The mass concentrations of non-refractive OA, nitrate, sulfate, ammonium and
157 chloride was measured by time-of-flight aerosol chemical speciation monitor with
158 extended resolution (ToF-ACSM X, Aerodyne). Instrument principles, calibration
159 procedures, and operational details for the ToF-ACSM X are described in a previous
160 study of ours (Zhang et al., 2025a). The aerosol extinction and scattering coefficient
161 (Fig. S3) at wavelength of 440, 530 and 630 nm were measured by Multi-Wavelength
162 Cavity Attenuated Phase Shift Single-Scattering Albedo Monitor (CAPS-ALB,
163 Shoreline) (Weber et al., 2022). Absorption was calculated as the difference between
164 extinction and scattering, with estimated uncertainties of ~1-10% for both extinction
165 and scattering (Modini et al., 2021), leading to a conservative absorption uncertainty of
166 ~15-20% for the submicron BC particles considered. No explicit truncation correction
167 was applied, as the analysis focuses on the relative enhancement of absorption with M_R
168 rather than absolute values. In this study, only the measurements at 630 nm were used
169 for subsequent analysis, as this wavelength is minimally affected by brown carbon
170 absorption. Besides, the aerosol scattering coefficient at wavelength of 450 nm, 525 nm,
171 and 635 nm was also measured by Multi Wavelength Integrating Nephelometer
172 (Abbreviation: Nephelometer, Aurora 3000, Acoem) (Schloesser, 2016). The slope of
173 the scattering coefficient measured by CAPS-ALB and Nephelometer at corresponding
174 wavelength was close to 1 (Fig. S4), indicating the all data are reliable for further
175 analysis. Besides, before sampling, the scattering coefficient of CAPS-ALB and
176 Nephelometer at every wavelength was calibrated using PSL spheres. Monodisperse
177 PSL particles of different diameters (100 nm, 150 nm, 200 nm and 300 nm) were
178 selected using a Differential Mobility Analyzer (DMA) and introduced into the
179 instruments, enabling accurate measurement of their scattering cross section (C_{sca}). The
180 slope of the C_{sca} measured by CAPS-ALB (or the Nephelometer) and modeled by Mie
181 theory was close to 1 (Fig. S5), indicating the reliability of the CAPS-ALB and
182 Nephelometer. The lower detection limit of the Nephelometer at all three wavelengths
183 was 0.3 Mm^{-1} with a 60-second integration time, while that of the CAPS-ALB was 1
184 Mm^{-1} with 30-second integration time.

185 **2.2 Mixing state and M_R -dependent optical transitions of the particle-resolved BC-** 186 **containing particles**

187 Under the assumption of singly charged particles, the mixing state of a single BC-
188 containing particle can be represented by the mass ratio of the BC coating to the BC

189 core, without relying on assumptions about particle morphology or coating structure,

$$M_R = (M_p - M_{BC_core}) / M_{BC_core} \quad (1)$$

190 where M_p and M_{BC_core} were the total mass and the BC core mass of each BC-containing
191 particle, respectively. Considering the uncertainties of M_p (5%) and M_{BC_core} (10%), the
192 uncertainty of M_R for a single BC-containing particle was approximately 11% (Text S2).
193 Then M_R was converted to the bulk-averaged M_R to be compared with the measured
194 E_{abs} in bulk particles by summing of total coating and BC core mass of BC-containing
195 particles each hour,

$$\text{bulk - averaged } M_R = \frac{\sum_i M_{R,i} \times M_{BC_core,i}}{\sum_i M_{BC_core,i}} \quad (2)$$

196 where i was the i^{th} single BC-containing particle. Propagating these uncertainties to the
197 hourly mass-weighted calculation resulted in an uncertainty of approximately 7% for
198 the bulk-averaged M_R (Text S2). The data measured by CPMA-SP2 were corrected via
199 several steps, including (1) correction of delay time, (2) multi-charged particles and (3)
200 collection efficiency (for details, see Text S1).

201 The M_R -dependent optical transitions of BC-containing particles were further
202 derived from SP2 measurements at a wavelength of 1064 nm. In the CPMA-SP2 system,
203 when both M_p and M_{BC_core} are known, the modeled scattering cross section ($C_{sca_modeled}$)
204 of BC-containing particles can be derived using Mie theory (Wang et al., 2021a). This
205 calculation assumes a core-shell structure, with the BC core having a refractive index
206 of 2.26-1.26*i* (Liu et al., 2017a; Zhao et al., 2020) and the non-absorbing coating
207 characterized by a refractive index of 1.48 and a density of 1.5 g cm⁻³ at a wavelength
208 of 1064 nm (Liu et al., 2015a). The measured scattering cross section ($C_{sca_measured}$) was
209 obtained from the SP2 using the leading-edge-only (LEO) technique, which
210 reconstructs the scattering signal as BC-containing particles pass through the SP2 laser
211 beam due to partial evaporation of refractory-absorbing material. The validity of this
212 reconstruction relies on the assumption that the leading-edge data used for fitting
213 represents an unperturbed particle, as extensively reported in previous studies (Liu et
214 al., 2014; Zhang et al., 2016; Brooks et al., 2019; Gao et al., 2007; Zhang et al., 2020).
215 Note only particles with successfully fitted LEO signals are considered in the optical
216 property calculations. By comparing $C_{sca_measured}$ with $C_{sca_modeled}$, the M_R -dependent
217 optical behavior of BC-containing particles can be inferred, particularly for transition-
218 state particles. This comparison captures how variations in coating-to-core mass ratio
219 influence scattering, providing observational constraints on the optical evolution of BC
220 during aging (Liu et al., 2017a; Liu et al., 2020). Further methodological details are
221 provided in Section 3.

222 2.3 The measured and modeled E_{abs}

223 The light absorption enhancement of BC-containing particles is defined as the ratio
224 of the mass absorption cross section (MAC) of the coated and uncoated BC-containing
225 particles (Eq. 3). Here, MAC is defined as the particle light absorption cross section
226 normalized by the BC mass, representing the light absorption per unit mass of BC.

$$E_{abs_measured} = \frac{MAC_{BC_coated_measured}}{MAC_{BC_core_measured}} \quad (3)$$

227 where $E_{abs_measured}$ is the measured light absorption enhancement, and
 228 $MAC_{BC_core_measured}$ is the mass absorption cross section for uncoated BC particles. The
 229 value of $MAC_{BC_core_measured}$ was obtained by extrapolating $MAC_{BC_coated_measured}$ to the
 230 limit of bulk-averaged $M_R = 0$ using linear regression. The $MAC_{BC_core_measured}$ at
 231 wavelength of 630 nm was $9.08 \pm 0.53 \text{ m}^2 \text{ g}^{-1}$ (mean \pm 90% confidence Interval) (Fig.
 232 S6). Based on our error propagation analysis, which accounts for measurement
 233 uncertainties in particle absorption and BC mass as well as the standard error of the
 234 extrapolation, the estimated uncertainty of $MAC_{BC_core_measured}$ is approximately 19-23%
 235 (Text S2). And the uncertainty of $E_{abs_measured}$ is approximately 26 - 32% (Text S2). Note
 236 the $MAC_{BC_core_measured}$ is slightly higher than the value of $7.5 \text{ m}^2 \text{ g}^{-1}$ recommended by
 237 Bond and Bergstrom (2006) but still within the range reported by other study ($\sim 6.5 - 17$
 238 $\text{m}^2 \text{ g}^{-1}$) (Zanatta et al., 2016), likely due to variations in measurement methods, and site-
 239 specific atmospheric conditions. Importantly, at high bulk-averaged M_R (≈ 5), the
 240 measured MAC did not approach the laboratory-based absorption enhancement (E_{abs}
 241 ≈ 2) reported for idealized core-shell soot particles (Cappa et al., 2012). The observed
 242 limited $E_{abs} \approx 1.1\sim 1.5$ is consistent with ambient studies and can be explained by the
 243 complexity of ambient particles: the heterogeneity of particle-resolved M_R and
 244 morphology can reduce absorption enhancement by $\sim 20\text{-}70\%$ relative to idealized
 245 internal mixtures (Huang et al., 2024; Cappa et al., 2019), while variations in coating
 246 composition and instrumental uncertainties contribute additional variability but are
 247 considered secondary factors. These high-time-resolution field measurements therefore
 248 provide quantitative constraints on BC E_{abs} under realistic atmospheric conditions,
 249 complementing laboratory studies and informing model evaluations of aerosol optical
 250 properties and regional radiative effects.

251 The commonly used models for calculating the optical properties of BC-
 252 containing particles include Core-shell Mie theory (Cappa et al., 2012), T-matrix (Wu
 253 et al., 2020), and discrete dipole approximation (DDA) (Kahnert and Kanngießer, 2020)
 254 and the generalized Mie Model (Kahnert and Kanngießer, 2020). Among them, T-
 255 matrix, and DDA fully account for detailed particle structure by incorporating three-
 256 dimensional parameters such as particle configuration and internal mixing state (Wu et
 257 al., 2020). In contrast, Core-shell Mie theory relies solely on the BC core size (D_c) and
 258 coating thickness (D_p/D_c). Given the measurement data available in this study, the Core-
 259 shell Mie theory was used to calculate the E_{abs} of BC-containing particles at a
 260 wavelength of 630 nm. The refractive index (RI) of BC and its coatings are assumed to
 261 be $n=1.85+0.71i$ and $n=1.5+0i$ at a wavelength of 630 nm (Liu et al., 2015a; Liu et al.,
 262 2014). The size of BC core and coating thickness was directly measured by CPMA-SP2
 263 tandem system. For the uniform core-shell assumption, the M_R of every D_c was equal
 264 to bulk-averaged M_R (Section 2.2), as described by Cappa et al. (2019) and Liu et al.
 265 (2017a). Then the particle-resolved Core-shell Mie theory was employed to calculate
 266 the MAC_{BC} of individual BC-containing particles. After obtaining the particle-resolved
 267 MAC, we can calculate the MAC of BC particle ensembles as

$$MAC_{BC_coated_modeled} = \frac{\sum_i MAC_{BC_coated_modeled,i} \times M_{BC_core,i}}{\sum_i M_{BC_core,i}} \quad (4)$$

268 where i denotes the i^{th} BC-containing particle, and $MAC_{BC_coated_modeled,i}$ and $M_{BC_core,i}$
 269 represent the particle-resolved modeled MAC of coated BC and the mass of the BC
 270 core, respectively. Then, the modeled E_{abs} of BC particle ensembles are calculated as
 271 the ratio of MAC_{BC_coated} to MAC_{BC_core} . Note that the MAC_{BC_core} here is calculated
 272 using the core-shell Mie model when $D_p / D_c = 1$.

273 To better characterize the influence of coating on the optical response of BC-
 274 containing particles, we derived a parameter based on the ratio between the SP2-
 275 measured scattering cross section ($C_{\text{sca_measured}}$) and the values calculated using the core-
 276 shell Mie model ($C_{\text{sca_modeled}}$) at 1064 nm. This ratio changes consistently with M_R ,
 277 providing an optical indicator of coating-induced variations in particle properties. An
 278 empirical $C_{\text{sca_measured}}-M_R$ relationship (Fig. 3d-f) was then developed using SP2
 279 observations, and subsequently applied to infer the MAC of transition-state BC-
 280 containing particles. The bulk-averaged MAC was obtained by integrating the inferred
 281 MAC over the entire BC population.

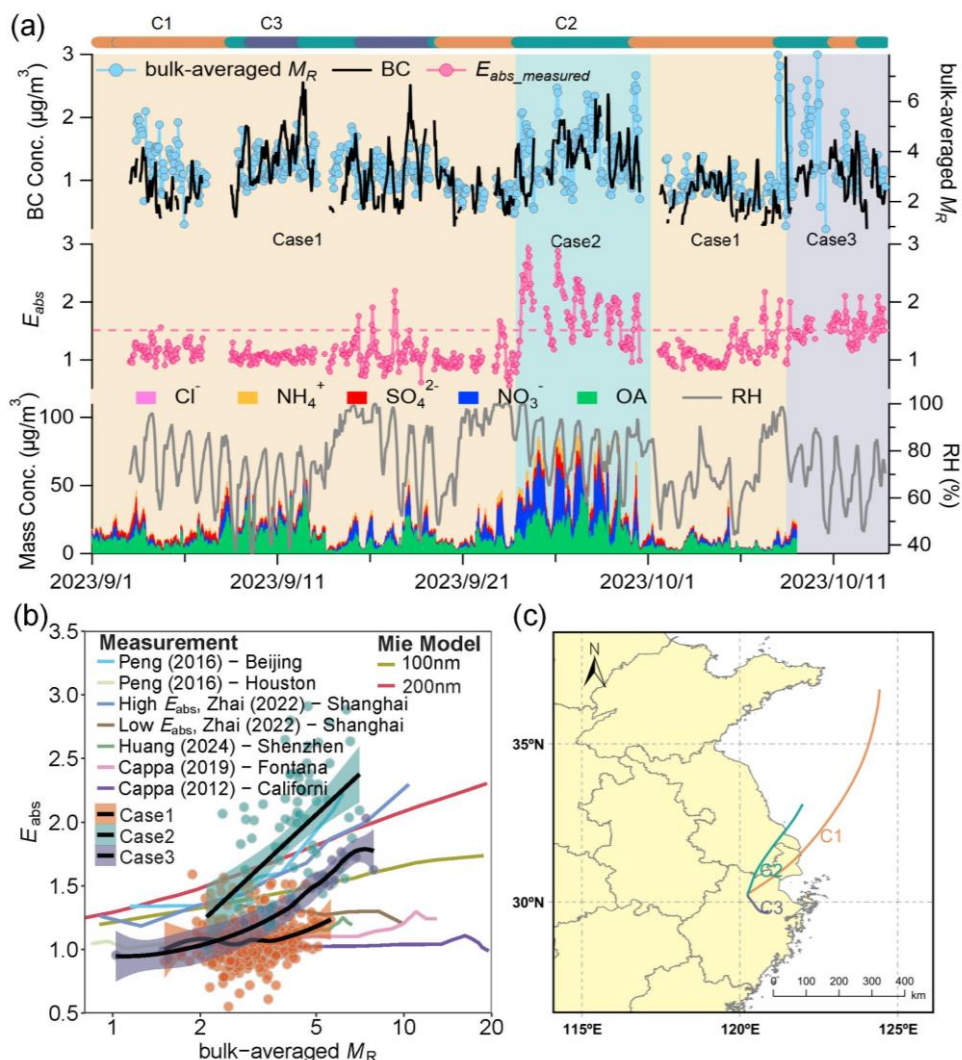
282 **3 Results and discussions**

283 **3.1 Direct observation of different E_{abs} .**

284 The average $E_{\text{abs_measured}}$ during the sampling period in Hangzhou is 1.28 ± 0.02 (mean
 285 $\pm 90\%$ confidence Interval, the same below) at wavelength of 630 nm, and the bulk-
 286 averaged M_R is 3.32 ± 0.06 , with average $E_{\text{abs_measured}}$ values of 1.09 ± 0.02 , 1.84 ± 0.07 ,
 287 and 1.55 ± 0.04 for Case 1, Case 2, and Case 3, respectively. To investigate the temporal
 288 evolution of BC coating, the observation period was classified into three cases based
 289 on the variation of $E_{\text{abs_measured}}$, using $E_{\text{abs}}=1.5$ as the reference threshold (Fig.1). Case
 290 1 (September 3-23 and October 1-7, 2023) corresponds to $E_{\text{abs_measured}}$ significantly
 291 below 1.5. These periods were characterized by relatively low non-refractory PM_{10}
 292 concentrations and high wind speeds ($WS = 0.94 \pm 0.04$ m/s). Back-trajectory analysis
 293 further shows that Case 1 was dominated by clean marine and nearby local air masses,
 294 resulting in relatively clean and weakly aged conditions (Fig. 1a). Case 2 (September
 295 24–30) corresponds to periods when $E_{\text{abs_measured}}$ remained continuously higher than 1.5.
 296 This episode occurred under stagnant meteorological conditions-characterized by weak
 297 winds ($WS = 0.81 \pm 0.02$ m/s) and elevated relative humidity ($RH = 81.34 \pm 17.12\%$) -
 298 that favored secondary aerosol formation. Back-trajectory analysis further indicates that
 299 Case 2 was dominated by air masses transported from Jiangsu and passing through
 300 northern Zhejiang, enhancing pollutant accumulation and promoting more aged BC
 301 conditions. Case 3 includes periods when $E_{\text{abs_measured}}$ persistently fluctuated around 1.5.
 302 The air masses during this period were a mixture of polluted inland outflow and clean
 303 marine inflow, suggesting the air masses were moderately aged-which explains the
 304 intermediate E_{abs} .

305 Some studies conducted in cities such as Beijing (Peng et al., 2016), Shanghai
 306 (Zhai et al., 2022) have observed a notable increase in $E_{\text{abs_measured}}$. In contrast, in cleaner
 307 regions like Shenzhen (Huang et al., 2024), Houston (Peng et al., 2016) and California

308 (Cappa et al., 2012; Cappa et al., 2019), even when R_{BC} reached approximately 5,
 309 $E_{abs_measured}$ often showed minimal enhancement. Our observations captured a wide
 310 range of $E_{abs_measured}$ values (0.92~1.84), encompassing high, medium, and low levels.
 311 In these three cases, $E_{abs_measured}$ exhibited distinct evolution patterns during the aging
 312 of BC-containing particles (Fig. 1), with its dependence on bulk-averaged M_R being
 313 minimal in Case 1, moderate in Case 3, and strongest in Case 2. The differences among
 314 the three cases may also be associated with variations in meteorological conditions, air
 315 mass origin, and chemical composition. On the other hand, in Case 2, the E_{abs} calculated
 316 using the traditional core-shell Mie model ($E_{abs_uniform}$) reasonably agrees with the
 317 $E_{abs_measured}$, whereas Case 3 shows a slightly lower level of consistency. However, in
 318 Case 1, the $E_{abs_uniform}$ predicted by the traditional core-shell Mie model is significantly
 319 higher than the $E_{abs_measured}$. In our subsequent analysis, we will address this discrepancy
 320 by exploring both heterogeneity of M_R and M_R -dependent transitions in optical
 321 properties.

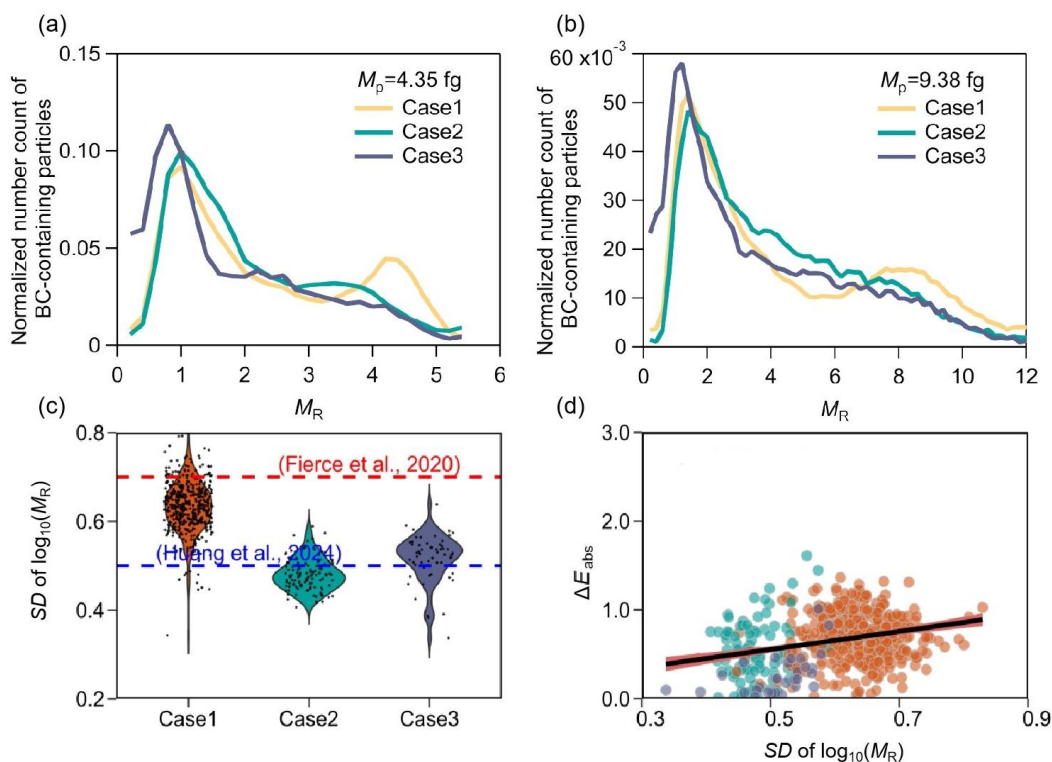


322
 323 **Figure. 1** (a) The time series of BC concentrations, bulk-averaged M_R , measured E_{abs} ,
 324 and the chemical components (including organics, nitrate, sulfate, ammonium and
 325 chloride) measured by TOF-ACSM X, as well as relatively humidity (RH). Shaded
 326 regions indicate different cases: light yellow for Case 1, blue-green for Case 2, and gray

327 for Case 3. (b) Comparison of measured E_{abs} in different observation periods and with
328 previous studies (Peng et al., 2016; Cappa et al., 2012; Zhai et al., 2022; Cappa et al.,
329 2019; Huang et al., 2024). The black solid line represents the fitted smoothing curve of
330 bulk-averaged M_R and measured E_{abs} , with the shaded area indicating the 95%
331 confidence interval of the fit. (c) Mean 48-h back-trajectory simulations initialized at
332 100 m above ground level. The back trajectories were calculated using the Hybrid
333 Single-Particle Lagrangian Integrated Trajectory (HYSPLIT) model driven by GDAS
334 meteorological fields.

335 **3.2 Role of mixing state heterogeneity in E_{abs} and direct evidence of M_R -dependent** 336 **optical transitions of BC-containing particles.**

337 The coating-to-BC mass ratio (M_R) and the ratio of measured to modeled scattering
338 cross sections were used to quantify the mixing state and associated optical transitions
339 behavior of BC-containing particles, with M_R serving as an important indicator of BC
340 aging (Zeng et al., 2024; Li et al., 2024; Liu et al., 2017a). Fig. 2a and 2b illustrated
341 significant differences in the normalized number distribution of BC-containing particles
342 at $M_p = 4.35$ fg and 9.38 fg during different observation periods. Specifically, during
343 Case 2 and Case 3, the M_R presents a unimodal distribution, with the peak value
344 increasing with increasing M_p . In contrast, during Case 1, the M_R exhibits a distinct
345 bimodal distribution, and both peak positions shift toward higher M_R values as M_p
346 increases. For example, when $M_p = 4.35$ fg, the two peaks occur at $M_R = 1$ fg and 4.2
347 fg, respectively, whereas at $M_p = 9.38$ fg, they shift to $M_R = 1.8$ fg and 8.0 fg,
348 respectively. The standard deviation (SD) of $\log_{10}(M_R)$ was used to characterize the
349 heterogeneity of M_R among individual BC-containing at each M_p . The results showed
350 that the SD of Case 1 (0.63 ± 0.004) was greater than that of Case 3 ($SD = 0.52 \pm 0.012$),
351 followed by Case 2 ($SD = 0.48 \pm 0.005$). In contrast, the $E_{\text{abs_measured}}$ exhibited an
352 opposite trend, suggesting that greater M_R heterogeneity of BC-containing particles
353 leads to a lower $E_{\text{abs_measured}}$. As shown in Fig. 2d, the discrepancy between the modeled
354 (uniform core-shell Mie model) and the measured E_{abs} increases with SD , with this trend
355 being most pronounced in Case 1, where M_R heterogeneity is highest. This suggests that
356 greater M_R heterogeneity may lead to larger deviations from the uniform core-shell
357 assumption, thereby increasing the mismatch between the modeled and measured E_{abs} .
358 Such discrepancies likely due to the uniform core-shell model's simplified treatment of
359 M_R heterogeneity in BC (Romshoo et al., 2024; Wang et al., 2021c).

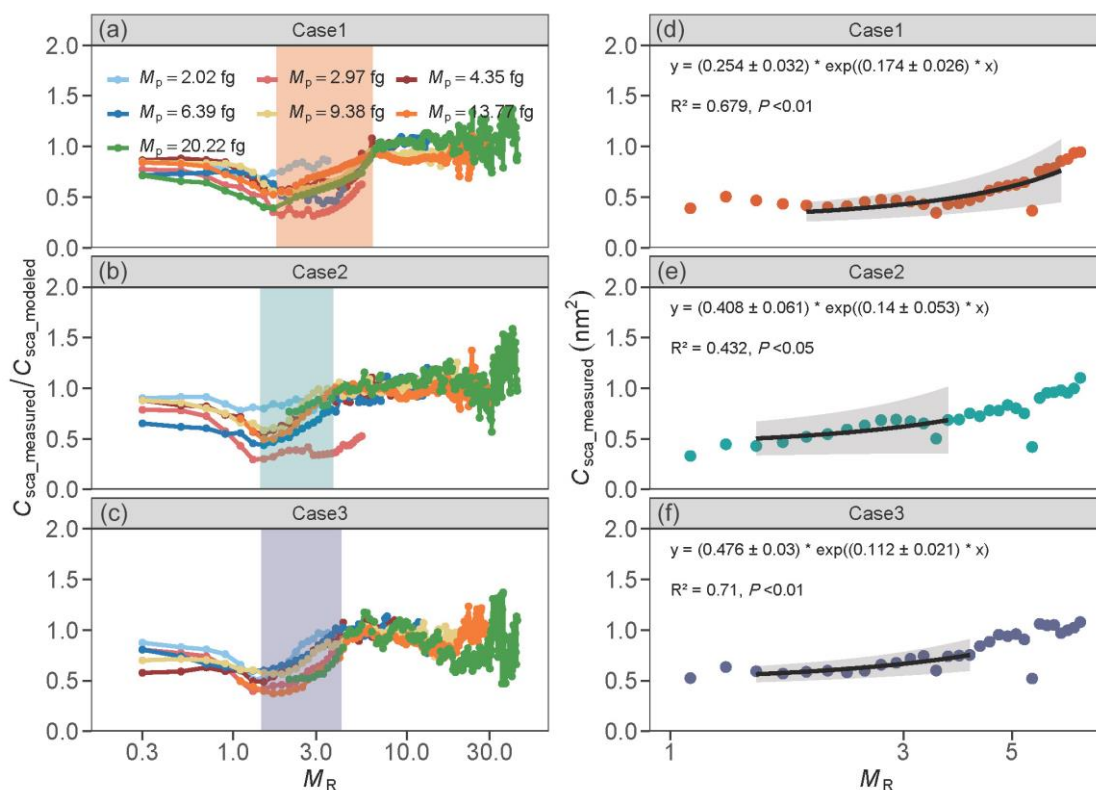


360

361 **Figure. 2** M_R heterogeneity of BC-containing particles in different observation periods.
 362 The average M_R normalized number distribution of BC-containing particles at $M_p =$
 363 4.35 fg (a) and $M_p = 9.38$ fg (b) during different cases. (c) Comparison of the average
 364 standard deviation (SD) of $\log_{10}(M_R)$ in this study with those reported by Huang et al.
 365 (2024) and Fierce et al. (2020), the SD characterizes the dispersion of M_R among
 366 individual BC-containing particles. (d) Linear fitting of ΔE_{abs} ($E_{\text{abs_uniform}} - E_{\text{abs_measured}}$)
 367 with the SD of $\log_{10}(M_R)$.

368 The SP2 measures the scattering cross-section (C_{sca}) of single BC-containing
 369 particles. The comparison between measured and the modeled (by Core-shell Mie
 370 model) C_{sca} serves as an optical proxy of changes in BC compaction and coating state,
 371 reflecting the evolution of optical properties during aging process. Fig. 3 presents the
 372 variation of the ratio $C_{\text{sca_measured}}/C_{\text{sca_modeled}}$ at wavelength of 1064 nm with M_R under
 373 different M_p . When M_R is relatively low, $C_{\text{sca_measured}}/C_{\text{sca_modeled}}$ is less than 1, suggesting
 374 that the BC cores may exist in a fractal structure, remain bare, or are not fully embedded
 375 in the coating materials. Consequently, the measured C_{sca} is lower than the C_{sca}
 376 predicted by the core-shell Mie model. This observation aligns with Liu et al. (2017a),
 377 who classified such BC-containing particles as externally mixed. As M_R increases,
 378 $C_{\text{sca_measured}}/C_{\text{sca_modeled}}$ also increases, indicating the BC particles becomes more
 379 compact and more thoroughly coated, transitioning toward a core-shell structure
 380 (Corbin et al., 2023). Following previous studies (Liu et al., 2017a; Liu et al., 2020),
 381 we describe this stage as a “transition state”. In this work, the transition state is neither
 382 defined by a fixed M_R threshold nor by any directly observed morphological boundary.
 383 Instead, it reflects an optically inferred state in which scattering enhancement increases
 384 markedly, with M_R ranges of 1.78-6.34 (Case 1), 1.43-3.78 (Case 2), and 1.45-4.19

385 (Case 3). The higher M_R thresholds observed in Case 2 and Case 3 indicate that under
 386 polluted conditions, BC particles can reach an optically core-shell-like state with
 387 comparatively less coating material. This likely reflected accelerated aging driven by
 388 enhanced secondary formation and condensation of inorganics and organics on BC,
 389 facilitated by stagnant meteorological conditions (low wind speed). Such conditions
 390 promote efficient coating growth on BC-containing particles, strengthening their light-
 391 absorption capability and leading to high E_{abs} . Therefore, compared with Case 1, BC in
 392 Case 2 and Case 3 required less coating material to reach the core-shell configuration.
 393 When M_R exceeds the transition state range, the ratio $C_{sca_measured}/C_{sca_modeled}$ becomes
 394 relatively stable, suggesting that the BC particles behave optically like compact,
 395 spherical core-shell structures.



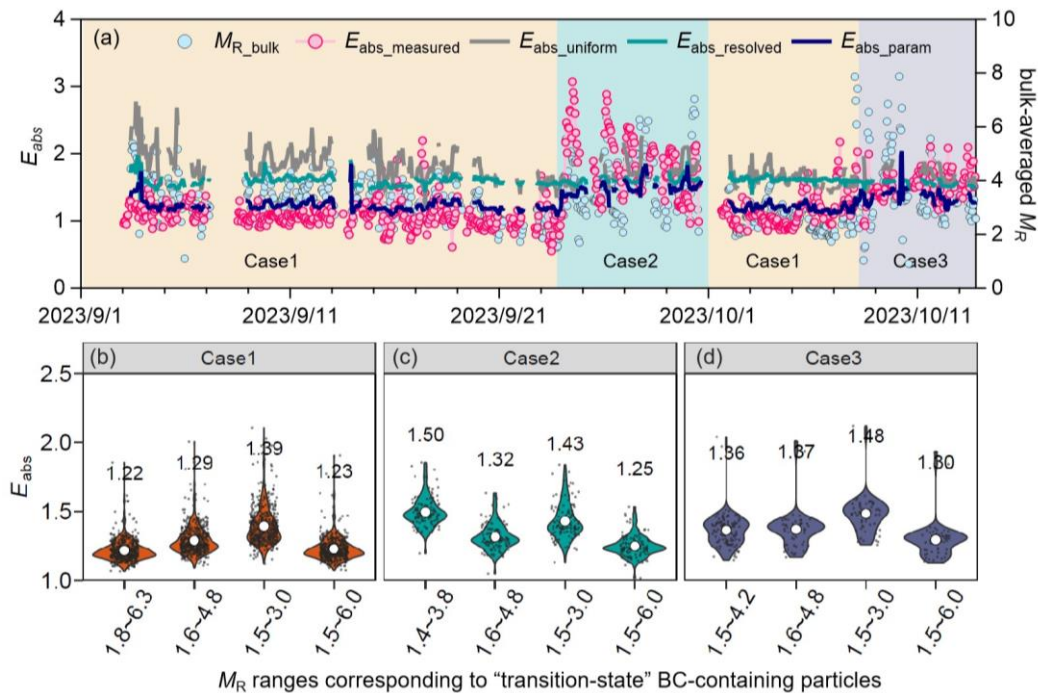
396

397 **Figure. 3** The optical behavior of BC-containing particles as a function of mass ratio
 398 (coating-to-BC, M_R). (a) – (c) show the ratio of measured to modeled scattering cross-
 399 section at the wavelength of 1064 nm during different cases. The shadows indicate the
 400 M_R ranges corresponding to “transition-state” BC-containing particles. (d) – (f) present
 401 the measured scattering cross-section as a function of M_R , along with fitted optical
 402 transition-dependent models representing the “transition-state” BC-containing particles.
 403 The fitted curves include the corresponding P-values, and the shaded areas denote the
 404 95% confidence intervals.

405 3.3 The predicted E_{abs} during different period.

406 The complexity of BC in the atmosphere depends on various factors, including the
 407 size, the coating amount, and the interaction between the BC core and its coating. In
 408 this study, comprehensive multidimensional information on single BC-containing

409 particle is retrieved and subsequently incorporated into the optical model, as shown in
 410 Fig. 4. The bias between $E_{\text{abs_uniform}}$ and $E_{\text{abs_measured}}$ varies across different periods, even
 411 when applying the same model input scheme. Specially, the $E_{\text{abs_uniform}}$ agrees with
 412 $E_{\text{abs_measured}}$ during Case 2 and Case 3, with deviations below 10%, whereas the
 413 deviation increases to as much as to 65% during Case 1, primarily due to the higher M_R
 414 dispersion of BC-containing particles in this period. To further investigate this
 415 discrepancy, we assume that all BC-containing particles adopt a core-shell structure and
 416 calculate the E_{abs} of each BC-containing particle based on the measured single-particle
 417 M_R . Subsequently, the E_{abs} of bulk BC-containing particles ($E_{\text{abs_resolved}}$) was determined
 418 and compared with $E_{\text{abs_measured}}$ to evaluate their consistency. The results show that for
 419 Case 1, although the discrepancy between the measured and modeled values exhibits a
 420 decreasing trend, the average deviation remains as high as 38%. This larger deviation,
 421 compared to previous particle-resolved modeling studies, is primarily attributed to the
 422 smaller dispersion of particle-to-particle M_R observed in Case 1 (Fig. 2c) relative to
 423 their model simulations (Fierce et al., 2020). However, for Case 2 and Case 3 with
 424 higher M_R heterogeneity of BC-containing particles, the error between the model and
 425 measured E_{abs} is almost negligible, with deviations below 10%, indicating that the core-
 426 shell Mie model can reproduce the observed E_{abs} during these periods. These findings
 427 further validate that the degree of M_R dispersion of BC-containing particles is a key
 428 factor in determining whether the core-shell Mie model overestimates the observed E_{abs} ,
 429 and to what extent this overestimation occurs.



430
 431 **Figure. 4** Comparison of measured and modeled E_{abs} under various different model
 432 input schemes. (a) shows the time series of the E_{abs} during the observation period. (b)
 433 – (d) were the sensitivity of E_{abs} to the “transition state” range of BC-containing
 434 particles. The “transition state” range of 1.6~4.8 was the average value derived from
 435 Case 1, Case 2 and Case 3. The range of 1.5~3.0 and 1.5~6.0 was reported by Liu et al.
 436 (2017a), and Liu et al. (2020), respectively.

437 The transitional-state particles are BC-containing particles in the process of
438 evolving from loosely aggregated fractal-like structures toward quasi-core-shell
439 configurations (Moffet et al., 2016; Moteki and Kondo, 2007). The abundance of
440 transitional-state particles varies notably under different atmospheric conditions,
441 directly influencing the measured E_{abs} (Liu et al., 2017a). During clean days (Case 1),
442 the atmospheric environment was characterized by low PM_{10} concentrations, weak
443 secondary formation, and highly variable coating conditions. Under such conditions,
444 our measurements show that BC-containing particles were dominated by transitional-
445 state structures (Fig. S9), representing the intermediate stage between externally mixed
446 aggregates and fully developed quasi-core-shell structures. The limited and
447 heterogeneous coating distribution on these particles substantially weakens the lensing
448 effect, resulting in lower measured E_{abs} (Peng et al., 2016). Because the core-shell Mie
449 model inherently assumes a uniform and concentric coating, it does not accurately
450 represent the optical behavior of these transitional particles, leading to a pronounced
451 overestimation of measured E_{abs} during Case 1. This indicates that, under clean
452 conditions, the optical properties of transitional-state particles are the key driver of the
453 model-observation discrepancy. In contrast, the haze period (Case 2) represents a more
454 aged and heavily coated aerosol environment and provides a useful reference for
455 understanding the factors influencing the measured E_{abs} . During Case 2, the high aerosol
456 loading and elevated bulk-averaged M_R were largely influenced by regional transport,
457 as air masses at 100 m, 500 m, and 1000 m all followed similar pathways from the
458 northern Yangtze River Delta into northern Zhejiang (Fig. 1c and Fig. S7). Stagnant
459 meteorological conditions, elevated relative humidity, and enhanced oxidative capacity
460 further facilitated vigorous liquid-phase and photochemical reactions, promoting the
461 abundant formation of secondary coatings on BC surfaces (Peng et al., 2016). Notably,
462 our observations show that E_{abs} increases systematically with the increasing
463 contribution of secondary nitrate (Fig. S8), consistent with the fact that nitrate-rich
464 conditions enhance aqueous-phase oxidation and accelerate the formation of thick
465 inorganic coatings (Liu et al., 2017b). As a result, a much larger fraction of BC-
466 containing particles exhibited internally mixed, quasi-core-shell structures rather than
467 transitional states (Fig. S9), which explains why the core-shell Mie model performs
468 substantially better for Case 2 than for Case 1. This contrast reinforces the central role
469 of transitional-state particles in determining measured E_{abs} when coatings are sparse,
470 irregular, or partially developed. Given the strong influence of transitional-state
471 particles on measured E_{abs} in Case 1, precise constraints on their optical behavior are
472 crucial for improving E_{abs} estimates across different atmospheric scenarios. To address
473 this, an empirical formula based on optical measurements was developed to estimate
474 the E_{abs} of BC-containing particles in the “transition state”, derived from fitting the
475 measured C_{sca} against M_R (Fig. 3d-3f). By applying this empirical formula to the
476 calculation of E_{abs} , the resulting value for Case 1 was 1.21 ± 0.01 . For Case 2 and Case
477 3, the E_{abs} calculated using the same formula ($E_{\text{abs_param}}$) remained slightly lower than
478 the $E_{\text{abs_measured}}$, but the deviation was within 20%, demonstrating the reliability of the
479 approach across different atmospheric conditions.

480 In recent years, particle-resolved models have been increasingly applied in field

481 observations to mitigate the well-known overestimation of E_{abs} by uniform core-shell
482 Mie model (Fierce et al., 2020; Li et al., 2024; Jiang et al., 2025). Some studies have
483 incorporated particle-specific structural detail using approaches such as the electron-
484 microscope-to-BC-simulation (EMBS) framework (Wang et al., 2021c; Wang et al.,
485 2021b; Chakrabarty et al., 2006), which further improves the representation of BC
486 absorption. In this study, we introduce an observationally constrained parameterization
487 that links SP2-measured scattering cross sections with core-shell Mie calculations. This
488 scheme identifies the optical transition state through following steps: (1) measuring
489 single-particle C_{sca} with SP2, (2) fitting the relationship between $C_{\text{sca_measured}}$ and M_{R}
490 (Fig. 4b-4c), (3) identifying the M_{R} range associated with transitional optical behavior
491 (“transition state”), and (4) inferring the MAC of transition-state particles using the
492 fitted relationship before integrating MAC over all particles to obtain bulk E_{abs} . This
493 parameterization improves agreement with observations, especially during clean
494 periods (Case 1), when the uniform core-shell assumption tends to produce the largest
495 discrepancies. However, its performance depends on correctly identifying the M_{R} range
496 of the transition state. Our results show that, in polluted periods (Cases 2 and 3), the M_{R}
497 range associated with the transition-state becomes relatively narrow, while under clean
498 conditions it tends to expand. Consequently, applying a fixed M_{R} threshold across all
499 atmospheric conditions can introduce systematic biases in modeled E_{abs} (Fig. 4b, c and
500 d). Although M_{R} heterogeneity alone can adequately reproduce E_{abs} during polluted
501 periods, adopting separate input schemes for different environments would complicate
502 radiative transfer calculations and limit broader applicability.

503 To address this issue, we emphasize that the proposed framework is adaptable to
504 environments in which BC particles undergo similar optical transitions. Key parameters,
505 including the M_{R} thresholds that define the transition state and other indicators derived
506 from the $C_{\text{sca_measured}}-M_{\text{R}}$ relationship, can be recalibrated for different atmospheric
507 contexts. This includes rural areas, biomass-burning regions, or seasons with distinct
508 pollution characteristics, where coating composition and aging processes may vary.
509 Although the parameterization is fundamentally based on the optical evolution of BC
510 from loosely coated to more compact states, it can be adjusted to account for local
511 differences in particle coating and aging dynamics. Thus, the unified scheme
512 incorporates both M_{R} variability and optical characteristics of transitional particles,
513 providing a flexible and physically consistent approach for a wide range of atmospheric
514 environments. Overall, this observationally constrained approach offers a more
515 consistent representation of BC mixing states across diverse atmospheric conditions,
516 thereby reducing uncertainties in optical modeling and enhancing the reliability of BC
517 radiative effect assessments.

518 **4 Conclusions**

519 In this study, we employed the CPMA-SP2 tandem system to investigate the mass
520 ratio of coating to core (M_{R}) of BC-containing particles in Hangzhou, China, and to
521 assess how M_{R} heterogeneity and optical transitions influence their E_{abs} under different
522 atmospheric conditions. By dividing the observation into three representative scenarios
523 (Case 1, Case 2, and Case 3), we identified significant differences in the measured E_{abs}

524 that are closely associated with the evolution and distribution of M_R . The results indicate
525 that both M_R heterogeneity and optical effects of BC-containing particles in the
526 transition state are critical for accurately modeling BC E_{abs} . During clean periods (Case
527 1), the uniform core-shell Mie model significantly overestimated E_{abs} , while during
528 polluted periods (Case 2 and Case 3), model predictions were more consistent with the
529 measured E_{abs} . To address these discrepancies, we developed an observationally
530 constrained parameterization for BC particles in the transition state based on the
531 transitional optical behavior. This scheme effectively reconciles modeled and measured
532 E_{abs} across different pollution scenarios, particularly in clean periods dominated by
533 externally mixed or partially coated BC-containing particles. These results highlight the
534 limitations of uniform model input schemes under complex atmospheric conditions and
535 underscore the value of a unified parameterization framework that accounts for both
536 M_R heterogeneity and the optical properties of transition-state particles. By
537 incorporating M_R -dependent optical transitions, this framework provides an adaptable
538 approach for representing BC mixing states and light absorption under different
539 atmospheric environments. This parameterization improves the consistency between
540 modeled and observed E_{abs} and reduces uncertainties in assessing the radiative effects
541 of BC-containing particles, offering a flexible tool for application to other atmospheric
542 conditions.

543 **Data availability.** The data are available from the link:
544 <http://doi.org/10.6084/m9.figshare.29097263>.

545 **Author contributions.**

546 Conceptualization: Jing Wei, Zhi-Bin Wang

547 Data curation: Jing Wei, Yao Song, Xiang-Yu Pei, Fei Zhang, Zheng-Ning Xu, Jin-Mei
548 Ding, Xiao-Yuan Wang, Sheng-Chen Xu, Xu-Dong Tian, Bing-Ye Xu

549 Formal analysis: Jing Wei

550 Funding acquisition: Zhi-Bin Wang, Bing-Ye Xu

551 Investigation: Zhi-Bin Wang

552 Methodology: Jing Wei, Zhi-Bin Wang

553 Visualization: Jing Wei, Zhi-Bin Wang

554 Writing – original draft: Jing Wei

555 **Competing interests.** At least one of the (co-)authors is a member of the editorial board
556 of *Atmospheric Chemistry and Physics*.

557

558 **Financial support.** This research was supported by the Joint Fund of Zhejiang
559 Provincial Natural Science Foundation of China (LZJMZ25D050003), the National
560 Key Research and Development Program of China (2022YFC3703505), the National
561 Natural Science Foundation of China (42305098), the China Postdoctoral Science
562 Foundation (2023M733028), the Key Laboratory of Formation and Prevention of
563 Urban Air Pollution Complex, Ministry of Ecology and Environment (2025080166).

564 **References**

- 565 Adachi, K. and Buseck, P. R.: Changes of ns-soot mixing states and shapes in an urban area during
566 CalNex, *Journal of Geophysical Research-Atmospheres*, 118, 3723-3730, 10.1002/jgrd.50321,
567 2013.
- 568 Adachi, K., Chung, S. H., and Buseck, P. R.: Shapes of soot aerosol particles and implications for their
569 effects on climate, *Journal of Geophysical Research: Atmospheres*, 115, D15206,
570 10.1029/2009jd012868, 2010.
- 571 Adachi, K., Moteki, N., Kondo, Y., and Igarashi, Y.: Mixing states of light-absorbing particles measured
572 using a transmission electron microscope and a single-particle soot photometer in Tokyo, Japan,
573 *Journal of Geophysical Research-Atmospheres*, 121, 9153-9164, 10.1002/2016jd025153, 2016.
- 574 Bauer, S. E., Ault, A. P., and Prather, K. A.: Evaluation of aerosol mixing state classes in the GISS
575 modelE-MATRIX climate model using single-particle mass spectrometry measurements, *Journal of*
576 *Geophysical Research: Atmospheres*, 118, 9834-9844, 10.1002/jgrd.50700, 2013.
- 577 Baumgardner, D., Popovicheva, O., Allan, J., Bernardoni, V., Cao, J., Cavalli, F., Cozic, J., Diapouli, E.,
578 Eleftheriadis, K., Genberg, P. J., Gonzalez, C., Gysel, M., John, A., Kirchstetter, T. W., Kuhlbusch,
579 T. A. J., Laborde, M., Lack, D., Müller, T., Niessner, R., Petzold, A., Piazzalunga, A., Putaud, J. P.,
580 Schwarz, J., Sheridan, P., Subramanian, R., Swietlicki, E., Valli, G., Vecchi, R., and Viana, M.: Soot
581 reference materials for instrument calibration and intercomparisons: a workshop summary with
582 recommendations, *Atmospheric Measurement Techniques*, 5, 1869-1887, 10.5194/amt-5-1869-
583 2012, 2012.
- 584 Beeler, P., Kumar, J., Schwarz, J. P., Adachi, K., Fierce, L., Perring, A. E., Katich, J. M., and Chakrabarty,
585 R. K.: Light absorption enhancement of black carbon in a pyrocumulonimbus cloud, *Nature*
586 *Communications*, 15, 10.1038/s41467-024-50070-0, 2024.
- 587 Bond, T. C. and Bergstrom, R. W.: Light Absorption by Carbonaceous Particles: An Investigative Review,
588 *Aerosol Science and Technology*, 40, 27-67, 10.1080/02786820500421521, 2006.
- 589 Brooks, J., Liu, D., Allan, J. D., Williams, P. I., Haywood, J., Highwood, E. J., Kompalli, S. K., Babu, S.
590 S., Satheesh, S. K., Turner, A. G., and Coe, H.: Black carbon physical and optical properties across
591 northern India during pre-monsoon and monsoon seasons, *Atmospheric Chemistry and Physics*, 19,
592 13079-13096, 10.5194/acp-19-13079-2019., 2019.
- 593 Cappa, C. D., Zhang, X., Russell, L. M., Collier, S., Lee, A. K. Y., Chen, C. L., Betha, R., Chen, S., Liu,
594 J., Price, D. J., Sanchez, K. J., McMeeking, G. R., Williams, L. R., Onasch, T. B., Worsnop, D. R.,
595 Abbatt, J., and Zhang, Q.: Light Absorption by Ambient Black and Brown Carbon and its
596 Dependence on Black Carbon Coating State for Two California, USA, Cities in Winter and Summer,
597 *Journal of Geophysical Research: Atmospheres*, 124, 1550-1577, 10.1029/2018JD029501, 2019.
- 598 Cappa, C. D., Onasch, T. B., Massoli, P., Worsnop, D. R., Bates, T. S., Cross, E. S., Davidovits, P., Hakala,
599 J., Hayden, K. L., Jobson, B. T., Kolesar, K. R., Lack, D. A., Lerner, B. M., Li, S.-M., Mellon, D.,
600 Nuaaman, I., Olfert, J. S., Petäjä, T., Quinn, P. K., Song, C., Subramanian, R., Williams, E. J., and
601 Zaveri, R. A.: Radiative Absorption Enhancements Due to the Mixing State of Atmospheric Black
602 Carbon, *Science*, 337, 1078-1081, <https://doi.org/10.1126/science.1223447>, 2012.
- 603 Chakrabarty, R. K., Moosmueller, H., Arnott, W. P., Garro, M. A., and Walker, J.: Structural and fractal
604 properties of particles emitted from spark ignition engines, *Environmental Science & Technology*,
605 40, 6647-6654, 10.1021/es060537y, 2006.
- 606 Chen, G., Liu, C., Wang, J., Yin, Y., and Wang, Y.: Accounting for Black Carbon Mixing State,

607 Nonsphericity, and Heterogeneity Effects in Its Optical Property Parameterization in a Climate
608 Model, *Journal of Geophysical Research: Atmospheres*, 129, e2024JD041135,
609 10.1029/2024JD041135, 2024.

610 China, S., Mazzoleni, C., Gorkowski, K., Aiken, A. C., Dubey, M. K., and Michigan Technological Univ,
611 H. M. I.: Morphology and mixing state of individual freshly emitted wildfire carbonaceous particles,
612 *Nature Communications*, 4, 2122-2122, 10.1038/ncomms3122, 2013.

613 Corbin, J. C., Modini, R. L., and Gysel-Ber, M.: Mechanisms of soot-aggregate restructuring and
614 compaction, *Aerosol Science and Technology*, 57, 89-111, 10.1080/02786826.2022.2137385, 2023.

615 Cross, E. S., Onasch, T. B., Ahern, A., Wrobel, W., Slowik, J. G., Olfert, J., Lack, D. A., Massoli, P.,
616 Cappa, C. D., Schwarz, J. P., Spackman, J. R., Fahey, D. W., Sedlacek, A., Trimborn, A., Jayne, J.
617 T., Freedman, A., Williams, L. R., Ng, N. L., Mazzoleni, C., Dubey, M., Brem, B., Kok, G.,
618 Subramanian, R., Freitag, S., Clarke, A., Thornhill, D., Marr, L. C., Kolb, C. E., Worsnop, D. R.,
619 and Davidovits, P.: Soot Particle Studies Instrument Inter-Comparison Project Overview, *Aerosol*
620 *Science and Technology*, 44, 592-611, 10.1080/02786826.2010.482113, 2010.

621 Fierce, L., Onasch, T. B., Cappa, C. D., Mazzoleni, C., China, S., Bhandari, J., Davidovits, P., Al Fischer,
622 D., Helgestad, T., Lambe, A. T., Sedlacek, A. J., Smith, G. D., Wolff, L., Brookhaven National Lab,
623 U. N. Y., and Pacific Northwest National Lab, R. W. A.: Radiative absorption enhancements by
624 black carbon controlled by particle-to-particle heterogeneity in composition, *Proceedings of the*
625 *National Academy of Sciences*, 117, 5196-5203, 10.1073/pnas.1919723117, 2020.

626 Gao, R. S., Schwarz, J. P., Kelly, K. K., Fahey, D. W., Watts, L. A., Thompson, T. L., Spackman, J. R.,
627 Slowik, J. G., Cross, E. S., Han, J. H., Davidovits, P., Onasch, T. B., and Worsnop, D. R.: A Novel
628 Method for Estimating Light-Scattering Properties of Soot Aerosols Using a Modified Single-
629 Particle Soot Photometer, *Aerosol Science and Technology*, 41, 125-135,
630 10.1080/02786820601118398, 2007.

631 Gysel, M., Laborde, M., Olfert, J. S., Subramanian, R., and Gröhn, A. J.: Effective density of Aquadag
632 and fullerene soot black carbon reference materials used for SP2 calibration, *Atmospheric*
633 *Measurement Techniques*, 4, 2851-2858, 10.5194/amt-4-2851-2011, 2011.

634 Huang, X.-F., Peng, Y., Wei, J., Peng, J., Lin, X.-Y., Tang, M.-X., Cheng, Y., Men, Z., Fang, T., Zhang,
635 J., He, L.-Y., Cao, L. M., Liu, C., Zhang, C., Mao, H., Seinfeld, J. H., and Wang, Y.: Microphysical
636 complexity of black carbon particles restricts their warming potential, *One Earth*, 7,
637 10.1016/j.oneear.2023.12.004, 2024.

638 Jiang, F., Zheng, Z., Coe, H., Healy, R. M., Poulain, L., Gros, V., Zhang, H., Li, W., Liu, D., West, M.,
639 Topping, D., and Riemer, N.: Integrating Simulations and Observations: A Foundation Model for
640 Estimating the Aerosol Mixing State Index, *Environmental Science & Technology Air*,
641 10.1021/acsestair.4c00329, 2025.

642 Kahnert, M. and Kanngießner, F.: Modelling optical properties of atmospheric black carbon aerosols,
643 *Journal of Quantitative Spectroscopy & Radiative Transfer*, 244, 106849,
644 10.1016/j.jqsrt.2020.106849, 2020.

645 Laborde, M., Schnaiter, M., Linke, C., Saathoff, H., Naumann, K. H., Möhler, O., Berlenz, S., Wagner,
646 U., Taylor, J. W., Liu, D., Flynn, M., Allan, J. D., Coe, H., Heimerl, K., Dahlkötter, F., Weinzierl,
647 B., Wollny, A. G., Zanatta, M., Cozic, J., Laj, P., Hitzenberger, R., Schwarz, J. P., and Gysel, M.:
648 Single Particle Soot Photometer intercomparison at the AIDA chamber, *Atmospheric Measurement*
649 *Techniques*, 5, 3077-3097, 10.5194/amt-5-3077-2012, 2012.

650 Li, W., Riemer, N., Xu, L., Wang, Y., Adachi, K., Shi, Z., Zhang, D., Zheng, Z., and Laskin, A.:

651 Microphysical properties of atmospheric soot and organic particles: measurements, modeling, and
652 impacts, *npj Climate and Atmospheric Science*, 7, 65, 10.1038/s41612-024-00610-8, 2024.

653 Liu, D., Taylor, J. W., Young, D. E., Flynn, M. J., Coe, H., and Allan, J. D.: The effect of complex black
654 carbon microphysics on the determination of the optical properties of brown carbon: BC
655 morphology on BrC optical properties, *Geophysical Research Letters*, 42, 613-619,
656 10.1002/2014GL062443, 2015a.

657 Liu, D., Allan, J. D., Young, D. E., Coe, H., Beddows, D., Fleming, Z. L., Flynn, M. J., Gallagher, M. W.,
658 Harrison, R. M., Lee, J., Prevot, A. S. H., Taylor, J. W., Yin, J., Williams, P. I., and Zotter, P.: Size
659 distribution, mixing state and source apportionment of black carbon aerosol in London during
660 wintertime, *Atmospheric Chemistry and Physics*, 14, 10061-10084, 10.5194/acp-14-10061-2014,
661 2014.

662 Liu, D., Whitehead, J., Alfarra, M. R., Reyes-Villegas, E., Spracklen, D. V., Reddington, C. L., Kong, S.,
663 Williams, P. I., Ting, Y.-C., Haslett, S., Taylor, J. W., Flynn, M. J., Morgan, W. T., McFiggans, G.,
664 Coe, H., and Allan, J. D.: Black-carbon absorption enhancement in the atmosphere determined by
665 particle mixing state, *Nature Geoscience*, 10, 184-188, 10.1038/ngeo2901, 2017a.

666 Liu, H., Pan, X., Liu, D., Liu, X., Chen, X., Tian, Y., Sun, Y., Fu, P., and Wang, Z.: Mixing characteristics
667 of refractory black carbon aerosols at an urban site in Beijing, *Atmospheric Chemistry and Physics*,
668 20, 5771-5785, 10.5194/acp-20-5771-2020, 2020.

669 Liu, H., Pan, X. L., Wang, D. W., Liu, X. Y., Tian, Y., Yao, W. J., Lei, S. D., Zhang, Y. T., Li, J., Lei, L.,
670 Xie, C. H., Fu, P. Q., Sun, Y. L., and Wang, Z. F.: Mixing characteristics of black carbon aerosols in
671 a coastal city using the CPMA-SP2 system, *Atmospheric Research*, 265,
672 10.1016/j.atmosres.2021.105867, 2022.

673 Liu, S., Aiken, A. C., Gorkowski, K., Dubey, M. K., Cappa, C. D., Williams, L. R., Herndon, S. C.,
674 Massoli, P., Fortner, E. C., Chhabra, P. S., Brooks, W. A., Onasch, T. B., Jayne, J. T., Worsnop, D.
675 R., China, S., Sharma, N., Mazzoleni, C., Xu, L., Ng, N. L., Liu, D., Allan, J. D., Lee, J. D., Fleming,
676 Z. L., Mohr, C., Zotter, P., Szidat, S., Prévôt, A. S. H., Los Alamos National Lab, L. A. N. M., and
677 Univ. of California, D. C. A.: Enhanced light absorption by mixed source black and brown carbon
678 particles in UK winter, *Nature Communications*, 6, 8435-8435, 10.1038/ncomms9435, 2015b.

679 Liu, Y., Wu, Z., Wang, Y., Xiao, Y., Gu, F., Zheng, J., Tan, T., Shang, D., Wu, Y., Zeng, L., Hu, M.,
680 Bateman, A. P., and Martin, S. T.: Submicrometer Particles Are in the Liquid State during Heavy
681 Haze Episodes in the Urban Atmosphere of Beijing, China, *Environmental Science & Technology*
682 *Letters*, 4, 427-432, 10.1021/acs.estlett.7b00352, 2017b.

683 Modini, R. L., Corbin, J. C., Brem, B. T., Irwin, M., Bertò, M., Pileci, R. E., Fetfatzis, P., Eleftheriadis,
684 K., Henzing, B., Moerman, M. M., Liu, F., Müller, T., and Gysel-Beer, M.: Detailed characterization
685 of the CAPS single-scattering albedo monitor (CAPS PMssa) as a field-deployable instrument for
686 measuring aerosol light absorption with the extinction-minus-scattering method, *Atmos. Meas.*
687 *Tech.*, 14, 819-851, 10.5194/amt-14-819-2021, 2021.

688 Moffet, R. C., O'Brien, R. E., Alpert, P. A., Kelly, S. T., Pham, D. Q., Gilles, M. K., Knopf, D. A., Laskin,
689 A., Pacific Northwest National Lab, R. W. A. E. M. S. L., Lawrence Berkeley National Lab, B. C.
690 A., and Stony Brook Univ, S. B. N. Y.: Morphology and mixing of black carbon particles collected
691 in central California during the CARES field study, *Atmospheric chemistry and physics*, 16, 14515-
692 14525, 10.5194/acp-16-14515-2016, 2016.

693 Moteki, N. and Kondo, Y.: Effects of Mixing State on Black Carbon Measurements by Laser-Induced
694 Incandescence, *Aerosol Science and Technology*, 41, 398-417, 10.1080/02786820701199728, 2007.

695 Moteki, N. and Kondo, Y.: Dependence of Laser-Induced Incandescence on Physical Properties of Black
696 Carbon Aerosols: Measurements and Theoretical Interpretation, *Aerosol Science and Technology*,
697 44, 663-675, 10.1080/02786826.2010.484450, 2010.

698 Naseri, A., Corbin, J. C., and Olfert, J. S.: Comparison of the LEO and CPMA-SP2 techniques for black-
699 carbon mixing-state measurements, *Atmos. Meas. Tech.*, 17, 3719-3738, 10.5194/amt-17-3719-
700 2024, 2024.

701 Naseri, A., Sipkens, T. A., Rogak, S. N., and Olfert, J. S.: An improved inversion method for determining
702 two-dimensional mass distributions of non-refractory materials on refractory black carbon, *Aerosol
703 Science and Technology*, 55, 104-118, 10.1080/02786826.2020.1825615, 2021.

704 Naseri, A., Sipkens, T. A., Rogak, S. N., and Olfert, J. S.: Optimized instrument configurations for tandem
705 particle mass analyzer and single particle-soot photometer experiments, *Journal of Aerosol Science*,
706 160, 10.1016/j.jaerosci.2021.105897, 2022.

707 Olfert, J. S. and Collings, N.: New method for particle mass classification - the Couette centrifugal
708 particle mass analyzer, *Journal of Aerosol Science*, 36, 1338-1352, 10.1016/j.jaerosci.2005.03.006,
709 2005.

710 Peng, J., Hu, M., Guo, S., Du, Z., Zheng, J., Shang, D., Zamora, M. L., Zeng, L., Shao, M., Wu, Y.-S.,
711 Zheng, J., Wang, Y., Glen, C. R., Collins, D. R., Molina, M. J., and Zhang, R.: Markedly enhanced
712 absorption and direct radiative forcing of black carbon under polluted urban environments,
713 *Proceedings of the National Academy of Sciences*, 113, 4266-4271, 10.1073/pnas.1602310113,
714 2016.

715 Qian, H., Xu, B., Xu, Z., Zou, Q., Zi, Q., Zuo, H., Zhang, F., Wei, J., Pei, X., Zhou, W., Jin, L., Tian, X.,
716 Zhao, W., and Wang, Z.: Anthropogenic Oxygenated Volatile Organic Compounds Dominate
717 Atmospheric Oxidation Capacity and Ozone Production via Secondary Formation of Formaldehyde
718 in the Urban Atmosphere, *ACS ES&T Air*, 2, 1033-1041, 10.1021/acsestair.4c00317, 2025.

719 Radney, J. G., You, R. A., Ma, X. F., Conny, J. M., Zachariah, M. R., Hodges, J. T., and Zangmeister, C.
720 D.: Dependence of Soot Optical Properties on Particle Morphology: Measurements and Model
721 Comparisons, *Environmental Science & Technology*, 48, 3169-3176, 10.1021/es4041804, 2014.

722 Romshoo, B., Müller, T., Ahlawat, A., Wiedensohler, A., Haneef, M. V., Imran, M., Warsi, A. B.,
723 Mandariya, A. K., Habib, G., and Pöhlker, M. L.: Significant contribution of fractal morphology to
724 aerosol light absorption in polluted environments dominated by black carbon (BC), *npj Climate and
725 Atmospheric Science*, 7, 87, 10.1038/s41612-024-00634-0, 2024.

726 Schloesser, H.: Use of a Multi-Wavelength Integrating Nephelometer to Determine Source Influences on
727 Particle Concentration Measurements. *Atmospheric optics: aerosols, visibility and the radiativ
728 balance 2016*, vol. 1: Atmospheric optics conference, 27-30 September 2016, Jackson Hole,
729 Wyoming, USA., 2016.

730 Schwarz, J. P., Katich, J. M., Lee, S. L., Thomson, D. S., and Watts, L. A.: "Invisible bias" in the single
731 particle soot photometer due to trigger deadtime, *Aerosol Science and Technology*, 56, 623-635,
732 10.1080/02786826.2022.2064265, 2022.

733 Seinfeld, J.: Atmospheric science - Black carbon and brown clouds, *Nature Geoscience*, 1, 15-16,
734 10.1038/ngeo.2007.62, 2008.

735 Stephens, M., Turner, N., and Sandberg, J.: Particle identification by laser-induced incandescence in a
736 solid-state laser cavity, *Applied Optics*, 42, 3726-3736, 10.1364/ao.42.003726, 2003.

737 Stier, P., Feichter, J., Kinne, S., Kloster, S., Vignati, E., Wilson, J., Ganzeveld, L., Tegen, I., Werner, M.,
738 Balkanski, Y., Schulz, M., Boucher, O., Minikin, A., and Petzold, A.: The aerosol-climate model

739 ECHAM5-HAM, *Atmospheric Chemistry and Physics*, 5, 1125-1156, 10.5194/acp-5-1125-2005,
740 2005.

741 Szopa, S., Naik, V., Adhikary, B., Artaxo, P., Bernsten, T., Collins, W. D., Fuzzi, S., Gallardo, L.,
742 Kiendler-Scharr, A., Klimont, Z., Liao, H., Unger, N., and Zanis, P.: Short-Lived Climate Forcers.
743 In *Climate Change 2021: The Physical Science Basis. Contribution of Working Group I to the Sixth*
744 *Assessment Report of the Intergovernmental Panel on Climate Change* (eds Masson-Delmotte, V.
745 et al.), IPCC, 2021.

746 Ueda, S., Nakayama, T., Taketani, F., Adachi, K., Matsuki, A., Iwamoto, Y., Sadanaga, Y., and Matsumi,
747 Y.: Light absorption and morphological properties of soot-containing aerosols observed at an East
748 Asian outflow site, Noto Peninsula, Japan, *Atmospheric chemistry and physics*, 16, 2525-2541,
749 10.5194/acp-16-2525-2016, 2016.

750 Wang, J., Wang, J., Cai, R., Liu, C., Jiang, J., Nie, W., Wang, J., Moteki, N., Zaveri, R. A., Huang, X.,
751 Ma, N., Chen, G., Wang, Z., Jin, Y., Cai, J., Zhang, Y., Chi, X., Holanda, B. A., Xing, J., Liu, T., Qi,
752 X., Wang, Q., Pöhlker, C., Su, H., Cheng, Y., Wang, S., Hao, J., Andreae, M. O., and Ding, A.:
753 Unified theoretical framework for black carbon mixing state allows greater accuracy of climate
754 effect estimation, *Nature Communications*, 14, 2703, 10.1038/s41467-023-38330-x, 2023.

755 Wang, T. T., Zhao, G., Tan, T. Y., Yu, Y., Tang, R. Z., Dong, H. B., Chen, S. Y., Li, X., Lu, K. D., Zeng,
756 L. M., Gao, Y. Q., Wang, H. L., Lou, S. R., Liu, D. T., Hu, M., Zhao, C. S., and Guo, S.: Effects of
757 biomass burning and photochemical oxidation on the black carbon mixing state and light absorption
758 in summer season, *Atmospheric Environment*, 248, 10.1016/j.atmosenv.2021.118230, 2021a.

759 Wang, Y., Pang, Y., Huang, J., Bi, L., Che, H., Zhang, X., and Li, W.: Constructing Shapes and Mixing
760 Structures of Black Carbon Particles With Applications to Optical Calculations, *Journal of*
761 *Geophysical Research: Atmospheres*, 126, 10.1029/2021jd034620, 2021b.

762 Wang, Y., Li, W., Huang, J., Liu, L., Pang, Y., He, C., Liu, F., Liu, D., Bi, L., Zhang, X., and Shi, Z.:
763 Nonlinear Enhancement of Radiative Absorption by Black Carbon in Response to Particle Mixing
764 Structure, *Geophysical Research Letters*, 48, 10.1029/2021gl096437, 2021c.

765 Weber, P., Petzold, A., Bischof, O. F., Fischer, B., Berg, M., Freedman, A., Onasch, T. B., and Bundke,
766 U.: Relative errors in derived multi-wavelength intensive aerosol optical properties using cavity
767 attenuated phase shift single-scattering albedo monitors, a nephelometer, and tricolour absorption
768 photometer measurements, *Atmospheric Measurement Techniques*, 15, 3279-3296, 10.5194/amt-
769 15-3279-2022, 2022.

770 Wu, Y., Cheng, T., and Zheng, L.: Light absorption of black carbon aerosols strongly influenced by
771 particle morphology distribution, *Environmental Research Letters*, 15, 94051, 10.1088/1748-
772 9326/aba2ff, 2020.

773 Zanatta, M., Gysel, N., Bukowiecki, T., Müller, E., and Weingartner: A European aerosol
774 phenomenology-5: Climatology of black carbon optical properties at 9 regional background sites
775 across Europe, *Atmospheric Environment*, 2016.

776 Zanatta, M., Bogert, P., Ginot, P., Gong, Y., Hoshyaripour, G. A., Hu, Y., Jiang, F., Laj, P., Li, Y., Linke,
777 C., Möhler, O., Saathoff, H., Schnaiter, M., Umo, N. S., Vogel, F., and Wagner, R.: AIDA Arctic
778 transport experiment – Part 1: Simulation of northward transport and aging effect on fundamental
779 black carbon properties, *Aerosol Research*, 3, 477-502, 10.5194/ar-3-477-2025, 2025.

780 Zeng, L., Tan, T., Zhao, G., Du, Z., Hu, S., Shang, D., and Hu, M.: Overestimation of black carbon light
781 absorption due to mixing state heterogeneity, *npj Climate and Atmospheric Science*, 7, 2,
782 10.1038/s41612-023-00535-8, 2024.

783 Zhai, J., Yang, X., Li, L., Bai, B., Liu, P., Huang, Y., Fu, T.-M., Zhu, L., Zeng, Z., Tao, S., Lu, X., Ye, X.,
784 Wang, X., Wang, L., and Chen, J.: Absorption Enhancement of Black Carbon Aerosols Constrained
785 by Mixing-State Heterogeneity, *Environmental Science & Technology*, 56, 1586-1593,
786 10.1021/acs.est.1c06180, 2022.

787 Zhang, F., Shen, J., Xu, D., Shen, J., Qin, Y., Shi, R., Wei, J., Xu, Z., Pei, X., Tang, Q., Chen, H., Xu, B.,
788 and Wang, Z.: Unveiling the key drivers and formation pathways for secondary organic aerosols in
789 an eastern China megacity, *Journal of Hazardous Materials*, 498, 10.1016/j.jhazmat.2025.139925,
790 2025a.

791 Zhang, J., Wang, Y., Teng, X., Liu, L., Xu, Y., Ren, L., Shi, Z., Zhang, Y., Jiang, J., Liu, D., Hu, M., Shao,
792 L., Chen, J., Martin, S. T., Zhang, X., and Li, W.: Liquid-liquid phase separation reduces radiative
793 absorption by aged black carbon aerosols, *Communications Earth & Environment*, 3, 128,
794 10.1038/s43247-022-00462-1, 2022.

795 Zhang, R. Y., Khalizov, A. F., Pagels, J., Zhang, D., Xue, H. X., and McMurry, P. H.: Variability in
796 morphology, hygroscopicity, and optical properties of soot aerosols during atmospheric processing,
797 *Proc. Natl. Acad. Sci. U. S. A.*, 105, 10291-10296, 10.1073/pnas.0804860105, 2008.

798 Zhang, Y., Zhang, Q., Cheng, Y., Su, H., Li, H., Li, M., Zhang, X., Ding, A., and He, K.: Amplification
799 of light absorption of black carbon associated with air pollution, *Atmospheric Chemistry and
800 Physics*, 18, 9879-9896, 10.5194/acp-18-9879-2018, 2018.

801 Zhang, Y., Zhang, Q., Cheng, Y., Su, H., Kecorius, S., Wang, Z., Wu, Z., Hu, M., Zhu, T., Wiedensohler,
802 A., and He, K.: Measuring the morphology and density of internally mixed black carbon with SP2
803 and VTDMA: new insight into the absorption enhancement of black carbon in the atmosphere,
804 *Atmospheric Measurement Techniques*, 9, 1833-1843, 10.5194/amt-9-1833-2016, 2016.

805 Zhang, Y. X., Zhang, Q., Yao, Z. L., and Li, H. Y.: Particle Size and Mixing State of Freshly Emitted
806 Black Carbon from Different Combustion Sources in China, *Environmental Science & Technology*,
807 54, 7766-7774, 10.1021/acs.est.9b07373, 2020.

808 Zhang, Z., Wang, J., Wang, J., Riemer, N., Liu, C., Jin, Y., Tian, Z., Cai, J., Cheng, Y., Chen, G., Wang,
809 B., Wang, S., and Ding, A.: Steady-state mixing state of black carbon aerosols from a particle-
810 resolved model, *Atmospheric Chemistry and Physics*, 25, 1869-1881, 10.5194/acp-25-1869-2025,
811 2025b.

812 Zhao, G., Shen, C., and Zhao, C.: Technical note: Mismeasurement of the core-shell structure of black
813 carbon-containing ambient aerosols by SP2 measurements, *Atmospheric Environment*, 243, 117885,
814 10.1016/j.atmosenv.2020.117885, 2020.

815